ACS APPLIED MATERIALS & INTERFACES

www.acsami.org

Research Article

# Universal Transfer Printing of Micelle-Templated Nanoparticles Using Plasma-Functionalized Graphene

Lok Shu Hui, Muhammad Munir, An Vuong, Michael Hilke, Victor Wong, Giovanni Fanchini, Markus Clark Scharber, Niyazi Serdar Sariciftci, and Ayse Turak*

Cite This: *ACS Appl. Mater. Interfaces* 2020, 12, 46530–46538

Read Online

ACCESS | Metrics & More | Article Recommendations | Supporting Information

**ABSTRACT:** Nanostructure incorporation into devices plays a key role in improving performance, yet processes for preparing two-dimensional (2D) arrays of colloidal nanoparticles tend not to be universally applicable, particularly for soft and oxygen-sensitive substrates for organic and perovskite-based electronics. Here, we show a method of transferring reverse micelle-deposited (RMD) nanoparticles (perovskite and metal oxide) on top of an organic layer, using a functionalized graphene carrier layer for transfer printing. As the technique can be applied universally to RMD nanoparticles, we used magnetic ($\gamma$-$Fe_2O_3$) and luminescent (methylammonium lead bromide ($MAPbBr_3$)) nanoparticles to validate the transfer-printing methodology. The strong photoluminescence from the $MAPbBr_3$ under UV illumination and high intrinsic field of the $\gamma$-$Fe_2O_3$ as measured by magnetic force microscopy (MFM), coupled with Raman measurements of the graphene layer, confirm that all components survive the transfer-printing process with little loss of properties. Such an approach to introducing uniform 2D arrays of nanoparticles onto sensitive substrates opens up new avenues to tune the device interfacial properties.

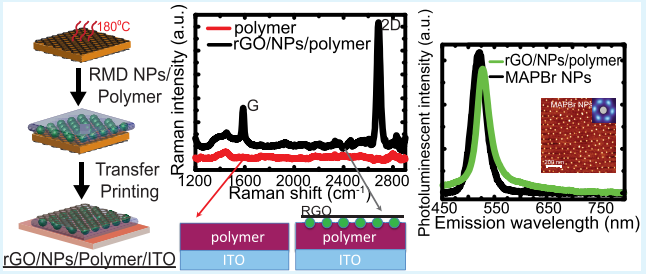


**KEYWORDS:** *transfer printing, graphene, nanoparticles, perovskites, plasma etching, Raman, photoluminescence*

## 1. INTRODUCTION

Incorporation of nanostructures into devices has been applied in a variety of advanced technological fields, including organic photovoltaics, displays, sensors, photonics, micromechanical systems, microfluidics, and microelectronics.[1−5] Nanostructures for nanopatterning used to enhance device performance can be from a wide variety of materials, including noble metals, metal alloys, metal oxides, and dielectric salts.[2,3,6−8]

Size monodispersity and control of two-dimensional (2D) order are particularly important when incorporating nanoparticles in optoelectronic devices, as heterogeneity is a key roadblock in the development of nanoparticle-based applications.[9] Uniformity is essential particularly in controlling the electrical properties such as charge transport and interfacial work function.[2,3,6,8] Reverse micelle templates formed by diblock copolymers offer a high degree of nanoparticle size control with 2D dispersion tuning, for a wide variety of materials.[10−13] However, processes for preparing such arrays of colloidal nanoparticles tend not to be universally suitable across the variety of substrates used in electronic devices. In particular, there is a need to use an oxygen or inert gas plasma to remove the polymer shell from around the nanoparticle. This poses a challenge for the integration of precise planar arrangements of colloidal nanoparticles into the device fabrication process of organic and perovskite electronics.

Nanotransfer printing methods using elastomer stamps have been successfully applied to move nanoparticles from a donor substrate to a soft target substrate.[1,14−18] Successful stamping transfer between the substrates depends strongly on the intrinsic surface energy differences between the stamp and the donor substrates,[19] surface roughness,[20] peeling velocity,[21,22] stamp mechanical properties,[23] and temperature and humidity.[17] Many approaches suffer from process-specific drawbacks, such as additional chemical treatments,[24−27] elevated temperatures,[28−30] or functionalization,[31] to successfully move nanoscale objects, hence no universal stamp method has yet been identified. Additionally, the introduction of surface discontinuities and/or contamination that can greatly hinder the properties and functions of the transferred materials is common with soft stamping.[18] A related approach is to use a sacrificial carrier layer with high mechanical strength. As defect-free, monolayer graphene is considered to be among the strongest materials tested,[32−34] it could be the ideal material for such an approach. Though transfer methods have been

**Received:** July 11, 2020
**Accepted:** September 17, 2020
**Published:** September 17, 2020

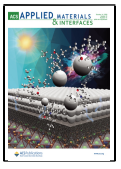

used to transfer large-area chemical vapor deposition (CVD)-grown graphene for graphene-based organic photovoltaics, field-effect transistors and resonators,[35−41] these approaches also generally suffer from polymer residue contamination from the stamp, or tears and wrinkles in the graphene layer, limiting their use.[37,40,41] Recently, Feng et al. reported a direct transfer method for CVD graphene on Cu using the target organic layer as the holder substrate, which avoids the process of having unnecessary organic contaminants.[42]

In this contribution, we discuss our modification of Feng's approach to successfully transfer reverse micelle-deposited (RMD) nanoparticles using functionalized graphene as a mechanical support. By treating CVD graphene with low-temperature annealing, we have created a universal carrier to transfer nanoparticles onto organic surfaces. The reduced graphene oxide (rGO)-like layer that results from plasma etching provides a mechanical and environmental barrier suitable to transfer a variety of nanoparticle types. To validate our transfer-printing methodology, two types of nanoparticles were used: magnetic $\gamma$-$Fe_2O_3$ nanoparticles and luminescent perovskite nanoparticles of methylammonium lead bromide ($MAPbBr_3$). Raman spectroscopy, photoluminescence spectroscopy, and magnetic force microscopy (MFM) confirmed the successful transfer and stabilization of the nanoparticles on an organic surface using the modified graphene.

## 2. EXPERIMENTAL SECTION

**2.1. Synthesis.** Graphene was synthesized by CVD on commercially available 25 $\mu$m copper foils (Alfa Aesar). The foils were first chemically treated with acetic acid and annealed for 4 h at 1078 °C under a flow of 8 sccm hydrogen gas to clean the copper surface. The growth temperature was maintained at 1078 °C during a 4 min CVD growth phase where gas flows of 1.2 sccm methane were introduced. To ensure the same aging of all samples, the graphene samples were taken from the same master, which was stored in a desiccator in vacuum. The samples were annealed on a hotplate (Barnstead Thermolyne Super-Nuova) at 180 °C for 60 min. The samples were allowed to cool before further processing.

Reverse micelles were prepared by dissolving various molecular weight poly(styrene-*b*-2-vinyl pyridine) diblock copolymers (Polymer Source), in reagent grade nonpolar solvents such as toluene and *o*-xylene, with a concentration of 3 g/L under continuous stirring. After confirmation of reverse micelle formation by atomic force microscopy (AFM), precursor salts and reactants were added to the reverse micelle solutions, with a time interval of 24 h to allow thorough infiltration of each precursor. Methylammonium lead bromide ($MAPbBr_3$) was formed by mixing 0.5 M precursor solutions of methylammonium bromide (MABr) in isopropanol (IPA) (Caledon, reagent grade) and $PbBr_2$ in *N*,*N*-dimethylformamide (DMF) (Sigma-Aldrich, 99.8%) sequentially in the micelle solution. Iron oxide was formed by loading anhydrous $FeCl_3$ (sublimed grade, >99.9%; Sigma-Aldrich) to the micelles and oxygen plasma etching to form $\gamma$-$Fe_2O_3$.[43] The final loaded reverse micelle solution was centrifuged to remove excess, noninfiltrated salt and stirred further to prevent coagulation. The solution was spin-coated onto annealed graphene samples or cleaned substrates for characterization and transfer.

Poly(3-hexylthiophene) (P3HT) and phenyl-$C_{61}$-butyric acid methyl ester (PCBM) solution was prepared by dissolving 0.0281 g of P3HT and 0.0169 g of PCBM in 2.66 $cm^3$ of chlorobenzene to achieve a 1:0.6 weight ratio of P3HT and PCBM. This solution was stirred for 6 h at 55 °C to achieve a clear solution. Twenty microlitres of the solution was spin-coated on indium tin oxide (ITO) and on top of the nanoparticles/modified graphene/Cu stack and annealed on the hotplate at 120 °C for 5 min to achieve a uniform P3HT/PCBM spin-coated layer. For PMMA samples, a 10 $\mu$L solution of poly(methyl methacrylate) (PMMA) was spin-coated directly on the top of nanoparticles/modified graphene stack/Cu.

Plasma etching was performed in a Harrick Plasma PDC-001 plasma cleaner system with a 13.56 MHz R.F. generator at 29.6 W. The plasma chamber was held at a base pressure of 70 mTorr prior to target gas filling. During etching, a gas flow rate of 30 sccm was maintained.

**2.2. Characterization.** Raman spectroscopy was performed by a Renishaw inVia spectrometer at 514 nm laser excitation. The laser power was set to 1 mW to minimize laser heating effects (see Supporting Information, Figure SI-1), and a 1800 lines per mm grating was used. The surface was visualized using a 20× objective on the integrated microscope. The baseline of the spectra was created and then subtracted to highlight the peaks of interest if necessary. In addition, the spectra were smoothed by a Savitzky−Golay function. The spectrum features were deconvoluted using Lorentzian line shape profiles to highlight the characteristic peaks of interest.

Photoluminescence (PL) measurements were performed using a 405 nm diode laser with laser power in the range of 11 mW (spot diameter 1−2 mm). The sample emission is collected with a lens and guided to the detection unit with an optical fiber. A long-pass filter (550 nm) removes the excitation light before the collected radiation is fed into a monochromator (Andor, Shamrock 303i, grating 500 nm blaze, 150 lines/mm) and detected with an intensified charge-coupled device (Andor, iStar A-DH320T-18U-73). The sample was introduced to the laser with an exposure time of 0.0237 s and a slit opening of 50 $\mu$m. The detection range is from 500 to 900 nm. The measurement was taken in a darkened environment to prevent stray light.

Scanning electron microscopy (SEM) micrographs were obtained with a FEI VERSA 3D using an accelerating voltage of 5 kV and a probe current of 12 pA. Atomic force microscopy (AFM) micrographs were collected using an Asylum MFP-3D instrument (Oxford Instruments, Asylum Research) in the alternating current (AC) mode under ambient environment. AFM probes (Oxford Instruments Asylum Research) with a spring constant of 26 N/m and a resonant frequency at 300 kHz were engaged in tapping mode for topography scan. The dispersion of the nanoparticles was analyzed using the disLocate package in Mathematica.[10]

Aperture-type scanning near field optical microscopy (SNOM) measurements were recorded using Witec Alpha 300S to acquire SNOM and AFM topography simultaneously at 532 nm excitation. Hollow AFM cantilevers (SNOM-C, NT-MDT Inc.) with the 90 nm tip aperture diameter were utilized to scan the sample in transmission mode, and topographical (AFM) and optical SNOM images were acquired simultaneously. The optical signal is collected by an inverted microscope and detected with a photomultiplier tube (Hamamatsu U64000) in photon counting mode.

Two-pass tapping-mode magnetic force microscopy (MFM) was acquired using a magnetic-coated silicon cantilever (budget sensors Multi75M-G). The sample is first scanned with the cantilever demagnetized at the interface of rGO: $\gamma$-$Fe_2O_3$ and bare P3HT/PCBM. After the first scan, the tip is removed and exposed to an external constant magnetic field and scanned over the same area on the sample to acquire amplitude and phase images for comparison.

## 3. RESULTS AND DISCUSSION

Diblock copolymers, due to their amphiphilic nature, spontaneously form core−corona micelles in selective solvents. Using these micelles as "nanoreactors" allows the formation of highly size controllable nanoparticles, with less than 2% deviation in the average particle diameter.[2,6,12,43,44] The other advantage of reverse micelle deposition (RMD) is the control over the 2D dispersion: highly ordered periodic arrays with varying spacing and organization are achieved with the simple tuning of deposition parameters.[10,12] To produce RMD nanoparticles, poly(styrene-*b*-2-vinyl pyridine) (PS-*b*-P2VP) diblock copolymer reverse micelles are formed in a nonpolar solvent. To introduce these nanoparticles on to the organic


https://dx.doi.org/10.1021/acsami.0c12178
ACS Appl. Mater. Interfaces 2020, 12, 46530−46538

surface, we utilized a transfer method based on a modified graphene layer acting as a mechanical support.

A schematic flow of the transfer-printing procedure, modified from Feng's study,[42] is shown in Figure 1. After

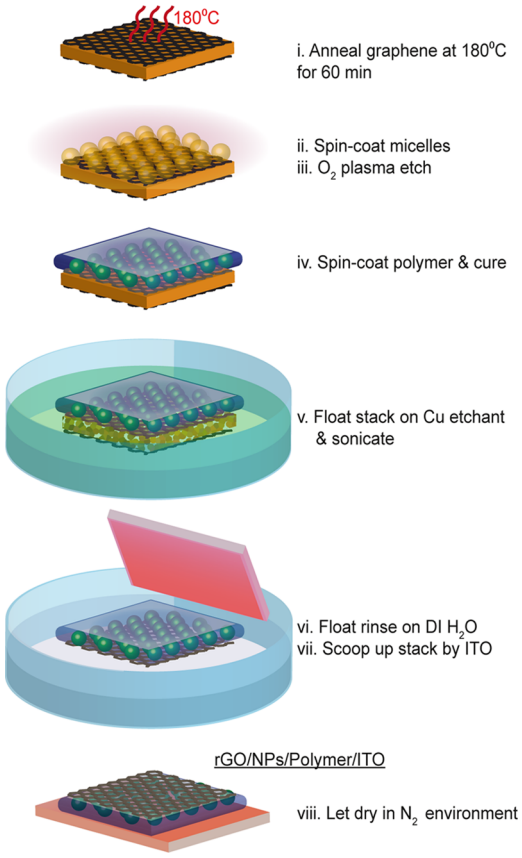


**Figure 1.** Schematic flow of the transfer-printing process: direct graphene transfer with the nanoparticles using a polymer holder. (i) Anneal CVD full graphene on Cu in air at 180 °C for 60 min. (ii) Spin-coat nanoparticle-loaded-micelle solutions on the annealed CVD full graphene on Cu. (iii) Plasma etch the whole stack in oxygen for 25 min to expose the nanoparticles from the micelles. (iv) Spin-coat polymer on the stack and cure. (v) Float the stack on Cu etchant solution to etch away the Cu layer, mildly agitated by sonication. (vi) Float the stack on deionized (DI) water three times to rinse off any Cu etchant residue. Displace water carefully with a syringe to avoid tearing of the stack from water surface tension. (vii) Scoop up the stack from the solution by lowering the substrate (ITO) on top of the stack. (viii) Flip the stack up-side-down and let it dry in a $N_2$ environment overnight. Final configuration of the stack: Reduced graphene oxide/nanoparticles/polymer/ITO.

the CVD graphene on Cu is annealed at 180 °C for 60 min, the reverse micelles loaded with precursors are spin-coated onto the graphene. The micelles together with CVD graphene are plasma-etched in oxygen to remove the polymeric shell, with the graphene transformed into a reduced graphene oxide (rGO)-like structure, as we have described previously.[45−47] For certain nanoparticles, the plasma is also used to convert the precursor into the desired material (e.g., iron chloride oxidizes to iron oxide). At this point, the target organic layer can be introduced by spin coating onto the composite layer, with thickness controlled by the spin-coating speed and concentration of the cast polymer.

After the target organic layer is cured according to the manufacturer's instructions, the whole stack of material will be floated onto a Cu etchant solution of 5 g/L ammonium peroxydisulfate to dissolve the copper foil. As CVD deposits graphene on both sides of the copper foil, the graphene layer grown at the bottom side of Cu needs to be removed. This happens spontaneously with our process because the etchant will also detach the graphene layer as Cu dissolves. Therefore, only the modified graphene is in contact with the Cu etchant, protecting the rest of the stack, including the organic deposit.[42,48]

The process is followed by displacing the Cu etchant with deionized water so that any Cu etchant residue can be washed away. The stack is subsequently retrieved, by lowering an ITO-coated-glass substrate on top of the stack and allowing the organic layer to attach. Finally, the stack is flipped to achieve the configuration of modified graphene/nanoparticles/organic layer/ITO and is allowed to dry in a $N_2$-filled glovebox environment. In this way, the nanoparticles should be trapped under the modified graphene layer. The post-transferred conditions of the graphene, nanoparticles, and target organic layers can be gauged either optically or spectroscopically As our printing process can be applied universally to nanoparticles produced by RMD, we were able to transfer the nanoparticles with properties that could be measured by various analytical techniques to confirm that all components are able to survive the transfer process.

The reverse micelle deposition (RMD) process requires sustained plasma etching to produce monodisperse nanoparticles with a high degree of two-dimensional order, as shown in Figure 2. Here, $MAPbBr_3$ nanoparticles are shown, but RMD is able to produce similar nanoparticle dispersions of a wide variety of materials under similar etching conditions[2,6,12,43,44] (see Figure SI-2 for AFM of $\gamma$-$Fe_2O_3$ nanoparticles produced under similar conditions as $MAPbBr_3$).

However, this level of etching is typically destructive to organic surfaces (see Supporting Information, Figure SI-3), preventing direct deposition on the organic surface. This same plasma dosage is also typically destructive to graphene.[46,49,50]

We have recently shown that CVD graphene on Cu behaves very differently under plasma compared to free-standing graphene and graphene supported on other substrates,[46] forming rGO-like structures under direct oxygen plasma bombardment. Due to the synergistic oxidation mechanism between graphene and the underlying Cu, the degree of oxygen functionalization of the activated graphene can be tuned with the oxygen plasma dose.[46]

The high plasma dose required to fully etch the nanoparticles will also completely etch as-deposited CVD graphene.[46] From our mechanistic insight on the interaction between plasma and graphene, we have found that it is possible to prevent the complete destruction of CVD graphene under plasma by preannealing at a low temperature (180 °C) to eliminate volatile surface contaminants.[45−47] A minimum of 4 min annealing is sufficient for a monolayer CVD graphene on Cu to withstand 25 min of plasma etching (ET25).[47] As prolonged low-temperature annealing does not introduce defects on the graphene, but does help to preserve a greater degree of intact $sp^2$ hybridization upon plasma exposure,[45,46] we chose an annealing time of 60 min (AT60), as shown in Figure 2a.

Before exposure to plasma, our CVD graphene shows the characteristic G and 2D peaks with the strong 2D signal


https://dx.doi.org/10.1021/acsami.0c12178
ACS Appl. Mater. Interfaces 2020, 12, 46530−46538

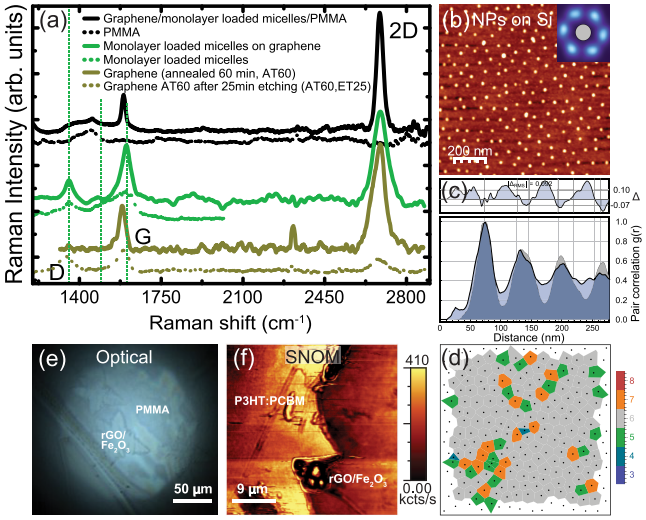


**Figure 2.** (a) Comparison of the Raman spectra of annealed graphene, loaded micelles on annealed graphene, and transferred loaded micelles on PMMA, showing characteristic peaks for graphene and complexated P2VP. The dashed green lines indicate the expected peak positions for the complexated P2VP peaks. Note that the peaks of graphene are offset from those of the complexated peaks by ~10 wavenumbers. A monolayer of the $FeCl_3$-loaded micelles on Al, the target PMMA substrate, and annealed graphene exposed to etching (showing both a D and a G peak) are also shown for comparison. (b) Atomic force micrographs of nanoparticle ($MAPbBr_3$) dispersion on silicon showing particle size uniformity and organization. The inset shows the entropic force map of the first neighbor. (c) Pair correlation function (pcf) of the nanoparticle dispersion from the AFM image in (b) showing hexatic packing of the particles (gray indicates pcf of simulated hexatic packing with the lattice disorder parameter to match the experimental results). Similar (d) Voronoi tessellation of the AFM image in (b) colored to show the number of nearest neighbors. The relatively few defects support the high degree of hexagonal packing. (e) Optical image of the modified graphene flakes with $\gamma$-$Fe_2O_3$ nanoparticles transfer-printed onto PMMA after etching. (f) Transmission SNOM image of the reduced graphene oxide-like flakes with $\gamma$-$Fe_2O_3$ transfer-printed onto the P3HT/PCBM layer after etching. In both cases, the flake edges are clearly visible and intact.

roughly twice that of the G peak, indicating high-quality defect-free monolayer graphene[51] (see Supporting Information, Table SI-1). The G peak at 1580 $cm^{-1}$ corresponds to the first-order degenerate phonon energy, $E_{2g}$ mode, at the G point. The 2D mode at 2690 $cm^{-1}$ comes from the G mode overtone and is indicative of $sp^2$ hybridization. After etching (dotted line bottom row, Figure 2a), a defect D mode (at 1354 $cm^{-1}$) and a broadened G mode with peak maxima at 1603 $cm^{-1}$ can be identified. The D mode is the defect-activated intervalley two-phonon mode for $sp^3$ defects.[51,52] The latter peak, also known as the $G_{app}$ mode resulting from the merging of the G mode and D′ mode,[53] can be deconvoluted into G at 1590 $cm^{-1}$ and D′ at 1606 $cm^{-1}$. The D′ is a defect-activated intravalley one-phonon mode associated with the CH $sp^3$ hybridization defect and the overtone of the D mode.[52] For defected graphene, the peak position difference of D′ to $G_{app}$ can be used to determine the nature of the graphene layer.[45,46] The peak position difference of 3 $cm^{-1}$ between $G_{app}$ and D′ mode indicates that the CVD graphene is oxygen-doped by the plasma to become rGO-like[46] (see Supporting Information, Figure SI-4 for peak fitting). The 2D mode (at 2790 $cm^{-1}$) is still visible after this etching step, implying a good degree of $sp^2$ hybridization.[45,46]

This suggests that the rGO-like layer is quite intact and should be strong enough to transfer the nanoparticles onto the target organic layer.

This can be seen in Figure 2e,f, showing the films transferred onto poly(methyl methacrylate) (PMMA) and poly(3-hexylthiophene)/[6,6]-phenyl-$C_{61}$-butyric acid methyl ester blend (P3HT/PCBM). As a proof of concept, partially grown CVD graphene on Cu (PG) was used with PMMA, as PG has a refractive index ($n$ = 2), which can provide an optical contrast from the background PMMA ($n$ = 1.49).[54,55] In such a way, one can optically identify spots where PG is transferred. In Figure 2e, the star-shaped rGO-like flakes are clearly visible and intact against the PMMA background. The annealing and plasma processing steps are able to form activated graphene without producing all of the material amorphization associated with conventional wet methods for GO and rGO syntheses.

Ideally, the nanoparticles should be sandwiched between the activated graphene layer and the target organic layer using this transfer method; however, as the nanoparticles formed by RMD are small, roughly 5−10 nm in size for the $MAPbBr_3$ and $\gamma$-$Fe_2O_3$ discussed here, and beneath the rGO-like structures, they are not optically resolvable. We used SNOM to try to visualize the particles, as it has both spatial and sub-superficial sensitivity.[56] In Figure 2f, the edge of the intact activated graphene flake is also observed in the SNOM micrograph for the transferred stack atop P3HT/PCBM. The SNOM signal in the flake region is modulated by light scattered due to the presence of clusters of nanoparticles beneath the rGO-like layer, whereas an rGO layer would be expected to be constant over the flake region (see Supporting Information, Figure SI-5).

Though the nonuniformity suggests that the nanoparticles exist beneath the rGO, it was not possible to spatially resolve the particles. Hence, it is still difficult to confirm a successful transfer using a direct imaging technique. As our transfer process can be applied universally to nanoparticles produced by RMD, we were able to transfer nanoparticles with properties that could be measured by various techniques to confirm that all components are able to survive the transfer process intact.

Raman spectroscopy is highly sensitive to graphene, but a monolayer (ML) of the nanoparticles or loaded micelles are normally not visible under Raman.[45,57] We have recently observed that the $FeCl_3$-loaded micelles show three distinctive peaks due to the complexation of Fe with the nitrogen in the vinyl pyridine moieties of 2VP.[43] On the metal substrates, it is possible due to surface enhancement to observe a monolayer of such micelles.

Figure 2a shows a ML of the $FeCl_3$-loaded micelles on annealed graphene, showing the expected complexation peaks around 1306, 1440, and 1591 $cm^{-1}$ (indicated by the dotted vertical lines and the dotted green spectrum for the loaded micelles on Al).[43] As there is only about a 10 $cm^{-1}$ difference between the Fe-2VP peak and the G peak of graphene, the graphene peak is buried as a shoulder in the spectrum due to the surface enhancement from the Cu substrate of the complexated micelle peaks (see Supporting Information, Figure SI-4 for peak deconvolution). However, the 2D peak from graphene is visible, showing the coexistence of both micelles and graphene after spin coating.

To measure the Raman spectrum of the transferred stack, again PMMA was used as the target organic surface as it


https://dx.doi.org/10.1021/acsami.0c12178
ACS Appl. Mater. Interfaces 2020, 12, 46530−46538

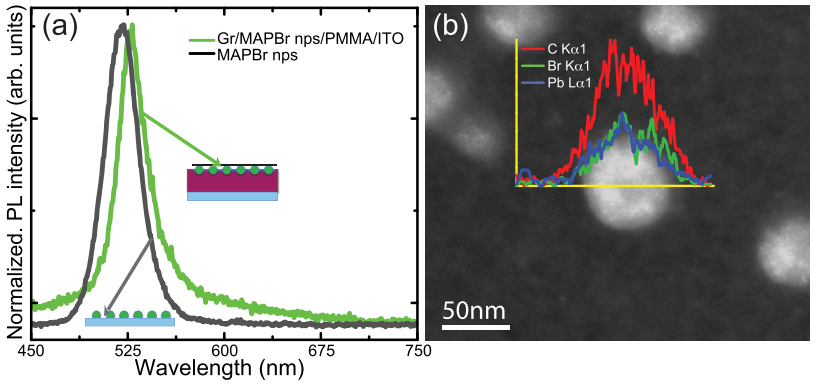


**Figure 3.** (a) Comparison of the normalized photoluminescence spectra of the $MAPbBr_3$ nanoparticles (black line) and $MAPbBr_3$ nanoparticles transferred onto PMMA (green line), measured with 405 nm laser excitation, showing the expected emission at 525 nm. (b) TEM image with the EDX line scan showing evidence of nanoparticle formation, displaying the composition of carbon (red line), lead (blue line), and bromine (green line) along the micelle diameter.

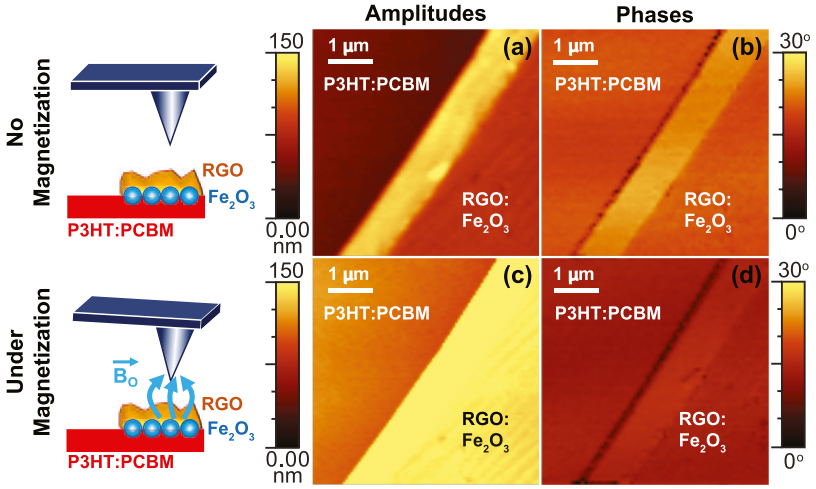


**Figure 4.** Magnetic force micrographs at the edge of the transfer-printed modified graphene/$Fe_2O_3$ nanoparticle composite stack. (a) Amplitude and (b) phase images before magnetizing the AFM tip. (c) Postmagnetizing topographic image and (d) postmagnetizing phase image at the graphene edge, showing a dramatic amplitude shift in correspondence with areas including $\gamma$-$Fe_2O_3$ nanoparticles, while no significant phase shift occurs in the area that is not rGO-$Fe_2O_3$ coated. This indicates that the nanoparticles have been magnetized, which is an important confirmation of their distribution underneath the activated graphene layer.

contains very few spectral features between 900 and 3000 $cm^{-1}$, as shown in Figure 2a (dotted black line), unlike P3HT/PCBM (see Supporting Information, Figure SI-6). Note that in this case, the micelles were not etched prior to transfer printing to observe the features from Fe complexation.

The Raman spectrum of the transferred stack (black curve, Figure 2a) shows a clear G mode and a strong 2D mode of the intact graphene, with only a small possible contribution from the $FeCl_3$-loaded micelles. The broad peak around 1400 $cm^{-1}$ is likely a convolution of the micelle-related peaks and the PMMA background. The broadband at the 1460 $cm^{-1}$ Raman shift region for PMMA is attributed to the asymmetric C−H stretching mode in the methyl group and methoxy group.[58−60] Though this is clear evidence of the successful transfer of defect-free high-quality graphene, it is still difficult to confirm the successful transfer of the micelles as the lack of signal from the complexation peaks may be due either to unsuccessful transfer or the loss of the surface-enhanced spectrum achievable on a metal substrate. To prove that the micelles are indeed transferred, it might be possible to produce a higher coverage of the nanoparticles that is above the Raman detection limit. However, as the thickness of the $FeCl_3$ reverse micelles is increased, the plasma etching required to completely remove the micelles is also increased, beyond that allowing an intact rGO layer. We have also observed that the etching action is escalated with increased micelles such that the graphene is severely damaged even with annealing.[57] Therefore, to prove that a single monolayer of particles can be successfully transferred, we have used luminescent organo-halide perovskite ($MAPbBr_3$) nanoparticles to take advantage of their strong photoluminescence (PL) response under UV illumination.

Figure 3a shows a comparison of the PL spectra of the $MAPbBr_3$ nanoparticles deposited on Si and the transferred stack of the $MAPbBr_3$ micelles. There is clearly an intense emission from $MAPbBr_3$ at around 525 nm, as expected. Figure 3b shows a TEM image of the $MAPbBr_3$ nanoparticles, with the inset energy-dispersive X-ray spectrometry (EDX) line profile showing the presence of C, Pb, and Br, confirming the successful formation of the $MAPbBr_3$ nanoparticles by RMD.[12]

The transferred nanoparticles also show a strong emission, with a bathochromic shift of 7 nm (from 521 to 528 nm). This shift could be due to a slight change in the particle size or it could be the result of some interaction with water during the


https://dx.doi.org/10.1021/acsami.0c12178
ACS Appl. Mater. Interfaces 2020, 12, 46530−46538

transfer process. Hydration and dehydration of the perovskite nanoparticles have been shown to cause hypsochromic or bathochromic shifts.[61−64] Lin et al.[48] recently predicted the water permeability of rGO as a function of the oxygen concentration. They found that below 25 atom % oxygen content, the water permeability was diminished due to the small pore size, with complete impermeability at around 17 atom % oxygen concentration.[48] The rGO produced through annealing and plasma etching from our earlier study has an oxygen content of 23.1 atom %,[46] so it is expected to act as a mostly impermeable barrier to water in the ambient glovebox environment.

Though there was some evidence of an emission shift due to hydration and a slight loss in intensity (~20%, see Supporting Information, Figure SI-7), the perovskite particles were not destroyed by the exposure to water. This is also important for the organic active layers such as P3HT/PCBM in organic devices. Figure SI-8 in the Supporting Information shows the stability of the rGO-nanoparticle stack on P3HT/PCBM, with the topography and optical characteristics unchanged over 4 months. Moisture is one of the key degradation factors for P3HT;[65,66] the rGO-like layer being able to block the direct contact of P3HT/PCBM with water during the Cu etching process is also an important criterion for its use in viable devices.

Photoluminescence provides strong evidence that the nanoparticles are sandwiched between the rGO-like layer and the polymer and are able to survive the many steps needed for successful transfer onto an organic surface. However, to preserve the PL, the $MAPbBr_3$ nanoparticles were not etched prior to transfer (though the graphene layer was etched). To show the coexistence of the nanoparticles and modified graphene, we took advantage of the fact that iron oxide nanoparticles formed from $FeCl_3$ using the RMD method can yield highly magnetic $\gamma$-$Fe_2O_3$ nanoparticles at room temperature[43,67] (see also Supporting Information, Figure SI-9 for magnetization and structural information of the $\gamma$-$Fe_2O_3$ nanoparticles). Oxygen plasma etching simultaneously removes the polymer shell and converts the precursor into iron oxide.

Successful transfer of the $\gamma$-$Fe_2O_3$ nanoparticles to the P3HT/PCBM active layer is confirmed by two-pass tapping-mode MFM, which can be seen in Figure 4. This shows the amplitude and phase micrographs collected simultaneously at the edge of the transfer-printed rGO/$Fe_2O_3$ nanoparticle layer with and without an applied magnetic field. Before magnetization, there is a clear boundary between the P3HT/PCBM layer and the transfer stack. The topography micrograph shows an intact rGO-like layer on the organic surface, both in amplitude and phase shift, though again the subsurface nanoparticles are not visible. Upon application of a magnetic field (Figure 4c), the amplitude map changes dramatically. The phase image (Figure 4d) confirms that there is no change in the real topography; therefore, the apparent change in amplitude must be proportional to the sample magnetization. As P3HT/PCBM and graphene are both nonmagnetic, this effect can only be attributed to the intrinsic magnetic field ($B_0$) of the $\gamma$-$Fe_2O_3$ nanoparticles, as shown in the schematic. Therefore, the particles, the rGO layer, and the polymer are all able to actively survive the transfer process.

## 4. CONCLUSIONS

In summary, we show the successful transfer of reverse micelle-templated nanoparticles using an rGO-like layer as a mechanical support onto organic surfaces (PMMA, P3HT/PCBM). Though no one technique was able to confirm that all of the components of the stack survived the transfer process, various characterization showed the unaffected performance of the stack components. The transfer results of the activated graphene are demonstrated by the post-transfer optical images and Raman measurements. The rGO-like structures transferred onto PMMA and P3HT/PCBM show a high level of intactness, which highlights the importance of preconditioning of graphene by low-temperature annealing. Evidence of the transferred nanoparticles sandwiched between the modified graphene and the organic layer is provided by the emission PL spectrum of the $MAPbBr_3$ nanoparticles. Intact rGO and active nanoparticles are proven by SNOM and MFM of magnetic iron oxide nanoparticles. By applying our approach to various target organic layers, and using a variety of RMD-produced nanoparticles, we show the universality of this transfer approach to introduce uniform nanoparticles onto oxygen-sensitive substrates.

## ■ ASSOCIATED CONTENT

### Supporting Information

The Supporting Information is available free of charge at https://pubs.acs.org/doi/10.1021/acsami.0c12178.

Effect of laser irradiation on the Raman spectrum of graphene; AFM micrographs of the nanoparticles from reverse micelle deposition and of various semiconducting organic layers exposed to prolonged plasma etching; Raman peak fitting analysis of the transfer stack components; SNOM micrographs of the transferred rGO-like flakes with the nanoparticles onto P3HT/PCBM; Raman spectra of P3HT/PCBM; non-normalized photoluminescence spectroscopy of the MAPBr nanoparticles; stability of UV−vis absorbance and topography of the transferred rGO-like film with the nanoparticles onto P3HT/PCBM; structural, composition, and magnetic properties of the reverse micelle-deposited iron oxide nanoparticles (PDF)

## ■ AUTHOR INFORMATION


### Corresponding Author

**Ayse Turak** − *Department of Engineering Physics, McMaster University, Hamilton L8S 4L7, Ontario, Canada;* orcid.org/0000-0002-2038-0624; Phone: +1 905 525-9140; Email: turaka@mcmaster.ca

### Authors

**Lok Shu Hui** − *Department of Engineering Physics, McMaster University, Hamilton L8S 4L7, Ontario, Canada;* orcid.org/0000-0003-0766-8153

**Muhammad Munir** − *Department of Engineering Physics, McMaster University, Hamilton L8S 4L7, Ontario, Canada;* orcid.org/0000-0003-1124-3844

**An Vuong** − *Department of Physics, McGill University, Montreal H3A 2T8, Quebec, Canada*

**Michael Hilke** − *Department of Physics, McGill University, Montreal H3A 2T8, Quebec, Canada;* orcid.org/0000-0002-2604-9377




https://dx.doi.org/10.1021/acsami.0c12178
ACS Appl. Mater. Interfaces 2020, 12, 46530−46538

**Victor Wong** − *Department of Physics and Astronomy, University of Western Ontario, London N6A 3K7, Ontario, Canada*

**Giovanni Fanchini** − *Department of Physics and Astronomy, University of Western Ontario, London N6A 3K7, Ontario, Canada;* orcid.org/0000-0002-2502-7475

**Markus Clark Scharber** − *Linz Institute for Organic Solar Cells (LIOS), Institute of Physical Chemistry, Johannes Kepler University, Linz 4040, Austria;* orcid.org/0000-0002-4918-4803

**Niyazi Serdar Sariciftci** − *Linz Institute for Organic Solar Cells (LIOS), Institute of Physical Chemistry, Johannes Kepler University, Linz 4040, Austria;* orcid.org/0000-0003-4727-1193

Complete contact information is available at: https://pubs.acs.org/10.1021/acsami.0c12178

### Notes

The authors declare no competing financial interest.

## ■ ACKNOWLEDGMENTS

The authors thank the MMRI for access to the AFM and Dr. Alex Adronov for the Raman instrument time. We gratefully acknowledge the financial support of the Austrian Science Foundation FWF within the Wittgenstein Prize (Z-222-N19) for N.S.S., the Canada Research Chair secretariat for G.F., the Ontario Ministry of Research and Innovation (ER15-11-123) for A.T., and the Natural Science and Engineering Research Council of Canada (RGPIN-2019-05994, 436100-2013 RGPIN, and 384889-2010 CREAT for A.T., RGPIN-2014-05004 and RGPIN-2020-56679 for G.F.). V.W. acknowledges an NSERC-PGS Scholarship.

## ■ REFERENCES

(1) Mizuno, H.; Kaneko, T.; Sakata, I.; Matsubara, K. Capturing by Self-Assembled Block Copolymer Thin Films: Transfer Printing of Metal Nanostructures on Textured Surfaces. *Chem. Commun.* **2014**, *50*, 362−364.

(2) Turak, A.; Aytun, T.; Ow-Yang, C. W. Solution Processed LiF Anode Modification for Polymer Solar Cells. *Appl. Phys. Lett.* **2012**, *100*, No. 253303.

(3) Aytun, T.; Turak, A.; Baikie, I.; Halek, G.; Ow-Yang, C. W. Solution-Processed LiF for Work Function Tuning in Electrode Bilayers. *Nano Lett.* **2012**, *12*, 39−44.

(4) Gu, X.; Qiu, T.; Zhang, W.; Chu, P. K. Light-Emitting Diodes Enhanced by Localized Surface Plasmon Resonance. *Nanoscale Res. Lett.* **2011**, *6*, No. 199.

(5) Atwater, H. A.; Polman, A. Plasmonics for Improved Photovoltaic Devices. *Nat. Mater.* **2010**, *9*, 205−213.

(6) Lee, S. I.; Yun, G. J.; Kim, J. W.; Hanta, G.; Liang, K.; Kojvic, L.; Hui, L. S.; Turak, A.; Kim, W. Y. Improved Hole Injection for Blue Phosphorescent Organic Light-Emitting Diodes Using Solution Deposited Tin Oxide Nano-Particles Decorated ITO Anodes. *Sci. Rep.* **2019**, *9*, No. 2411.

(7) Kim, T.-H.; Chung, D.-Y.; Ku, J.; Song, I.; Sul, S.; Kim, D.-H.; Cho, K.-S.; Choi, B. L.; Min Kim, J.; Hwang, S.; Kim, K. Heterogeneous Stacking of Nanodot Monolayers by Dry Pick-and-Place Transfer and Its Applications in Quantum Dot Light-Emitting Diodes. *Nat. Commun.* **2013**, *4*, No. 2637.

(8) Kim, T.-H.; Cho, K.-S.; Lee, E. K.; Lee, S. J.; Chae, J.; Kim, J. W.; Kim, D. H.; Kwon, J.-Y.; Amaratunga, G.; Lee, S. Y.; Choi, B. L.; Kuk, Y.; Kim, J. M.; Kim, K. Full-Colour Quantum Dot Displays Fabricated by Transfer Printing. *Nat. Photonics* **2011**, *5*, 176−182.

(9) Stavis, S. M.; Fagan, J. A.; Stopa, M.; Liddle, J. A. Nanoparticle Manufacturing − Heterogeneity through Processes to Products. *ACS Appl. Nano Mater.* **2018**, *1*, 4358−4385.

(10) Bumstead, M.; Liang, K.; Hanta, G.; Hui, L. S.; Turak, A. disLocate: Tools to Rapidly Quantify Local Intermolecular Structure to Assess Two-Dimensional Order in Self-Assembled Systems. *Sci. Rep.* **2018**, *8*, No. 1554.

(11) Kästle, G.; Boyen, H.-G.; Weigl, F.; Lengl, G.; Herzog, T.; Ziemann, P.; Riethmüller, S.; Mayer, O.; Hartmann, C.; Spatz, J.; Möller, M.; Ozawa, M.; Banhart, F.; Garnier, M.; Oelhafen, P. Micellar Nanoreactors — Preparation and Characterization of Hexagonally Ordered Arrays of Metallic Nanodots. *Adv. Funct. Mater.* **2003**, *13*, 853−861.

(12) Hui, L. S.; Beswick, C.; Getachew, A.; Heilbrunner, H.; Liang, K.; Hanta, G.; Arbi, R.; Munir, M.; Dawood, H.; Isik Goktas, N.; LaPierre, R. R.; Scharber, M. C.; Sariciftci, N. S.; Turak, A. Reverse Micelle Templating Route to Ordered Monodispersed Spherical Organo-Lead Halide Perovskite Nanoparticles for Light Emission. *ACS Appl. Nano Mater.* **2019**, *2*, 4121−4132.

(13) Qi, L. *Encyclopedia of Surface and Colloid Science*, 2nd ed.; Somasundaran, P.; Hubbard, A., Eds.; Taylor & Francis: London, 2006; pp 6183−6207.

(14) Rojas, J. P.; Torres Sevilla, G. A.; Alfaraj, N.; Ghoneim, M. T.; Kutbee, A. T.; Sridharan, A.; Hussain, M. M. Nonplanar Nanoscale Fin Field Effect Transistors on Textile, Paper, Wood, Stone, and Vinyl via Soft Material-Enabled Double-Transfer Printing. *ACS Nano* **2015**, *9*, 5255−5263.

(15) Carlson, A.; Bowen, A. M.; Huang, Y.; Nuzzo, R. G.; Rogers, J. A. Transfer Printing Techniques for Materials Assembly and Micro/Nanodevice Fabrication. *Adv. Mater.* **2012**, *24*, 5284−5318.

(16) Xia, Y.; Whitesides, G. M. Soft Lithography. *Annu. Rev. Mater. Sci.* **1998**, *28*, 153−184.

(17) Abkenar, S. K.; Tufani, A.; Ince, G. O.; Kurt, H.; Turak, A.; Ow-Yang, C. W. Transfer Printing Gold Nanoparticle Arrays by Tuning the Surface Hydrophilicity of Thermo-Responsive Poly N-Isopropylacrylamide (pNIPAAm). *Nanoscale* **2017**, *9*, 2969−2973.

(18) Linghu, C.; Zhang, S.; Wang, C.; Song, J. Transfer Printing Techniques for Flexible and Stretchable Inorganic Electronics. *Npj Flexible Electron.* **2018**, *2*, 1−14.

(19) Hur, S. H.; Khang, D. Y.; Kocabas, C.; Rogers, J. A. Nanotransfer Printing by Use of Noncovalent Surface Forces: Applications to Thin-Film Transistors That Use Single-Walled Carbon Nanotube Networks and Semiconducting Polymers. *Appl. Phys. Lett.* **2004**, *85*, 5730−5732.

(20) Bietsch, A.; Michel, B. Conformal Contact and Pattern Stability of Stamps Used for Soft Lithography. *J. Appl. Phys.* **2000**, *88*, 4310−4318.

(21) Klauk, H.; Halik, M.; Zschieschang, U.; Schmid, G.; Radlik, W.; Weber, W. High-Mobility Polymer Gate Dielectric Pentacene Thin Film Transistors. *J. Appl. Phys.* **2002**, *92*, 5259−5263.

(22) Meitl, M. A.; Zhu, Z. T.; Kumar, V.; Lee, K. J.; Feng, X.; Huang, Y. Y.; Adesida, I.; Nuzzo, R. G.; Rogers, J. A. Transfer Printing by Kinetic Control of Adhesion to an Elastomeric Stamp. *Nat. Mater.* **2006**, *5*, 33−38.

(23) Odom, T. W.; Love, J. C.; Wolfe, D. B.; Paul, K. E.; Whitesides, G. M. Improved Pattern Transfer in Soft Lithography Using Composite Stamps. *Langmuir* **2002**, *18*, 5314−5320.

(24) Bhattacharya, S.; Datta, A.; Berg, J. M.; Gangopadhyay, S. Studies on Surface Wettability of Poly(Dimethyl) Siloxane (PDMS) and Glass under Oxygen-Plasma Treatment and Correlation with Bond Strength. *J. Microelectromech. Syst.* **2005**, *14*, 590−597.

(25) Berthier, E.; Young, E. W. K.; Beebe, D. Engineers Are from PDMS-Land, Biologists Are from Polystyrenia. *Lab Chip* **2012**, *12*, 1224−1237.

(26) Tsougeni, K.; Vourdas, N.; Tserepi, A.; Gogolides, E.; Cardinaud, C. Mechanisms of Oxygen Plasma Nanotexturing of Organic Polymer Surfaces: From Stable Super Hydrophilic to Super Hydrophobic Surfaces. *Langmuir* **2009**, *25*, 11748−11759.

(27) Li, H.; Wu, J.; Huang, X.; Yin, Z.; Liu, J.; Zhang, H. A Universal, Rapid Method for Clean Transfer of Nanostructures onto Various Substrates. *ACS Nano* **2014**, *8*, 6563−6570.
(28) Thanh, Q. N.; Jeong, H.; Kim, J.; Kevek, J. W.; Ahn, Y. H.; Lee, S.; Minot, E. D.; Park, J.-Y. Transfer-Printing of As-Fabricated Carbon Nanotube Devices onto Various Substrates. *Adv. Mater.* **2012**, *24*, 4499−4504.
(29) Liang, X.; Sperling, B. A.; Calizo, I.; Cheng, G.; Hacker, C. A.; Zhang, Q.; Obeng, Y.; Yan, K.; Peng, H.; Li, Q.; Zhu, X.; Yuan, H.; Hight Walker, A. R.; Liu, Z.; Peng, L.-m.; Richter, C. A. Toward Clean and Crackless Transfer of Graphene. *ACS Nano* **2011**, *5*, 9144−9153.
(30) Reina, A.; Son, H.; Jiao, L.; Fan, B.; Dresselhaus, M. S.; Liu, Z.; Kong, J. Transferring and Identification of Single- and Few-Layer Graphene on Arbitrary Substrates. *J. Phys. Chem. C* **2008**, *112*, 17741−17744.
(31) Mizuno, H.; Buriak, J. M. Nanoscale Patterning of Organic Monolayers by Catalytic Stamp Lithography: Scope and Limitations. *ACS Appl. Mater. Interfaces* **2009**, *1*, 2711−2720.
(32) Lee, C.; Wei, X.; Kysar, J. W.; Hone, J. Measurement of the Elastic Properties and Intrinsic Strength of Monolayer Graphene. *Science* **2008**, *321*, 385−388.
(33) Papageorgiou, D. G.; Kinloch, I. A.; Young, R. J. Mechanical Properties of Graphene and Graphene-Based Nanocomposites. *Prog. Mater. Sci.* **2017**, *90*, 75−127.
(34) Zandiatashbar, A.; Lee, G.-H.; An, S. J.; Lee, S.; Mathew, N.; Terrones, M.; Hayashi, T.; Picu, C. R.; Hone, J.; Koratkar, N. Effect of Defects on the Intrinsic Strength and Stiffness of Graphene. *Nat. Commun.* **2014**, *5*, No. 3186.
(35) Liu, Z.; Liu, Q.; Huang, Y.; Ma, Y.; Yin, S.; Zhang, X.; Sun, W.; Chen, Y. Organic Photovoltaic Devices Based on a Novel Acceptor Material: Graphene. *Adv. Mater.* **2008**, *20*, 3924−3930.
(36) Liang, X.; Fu, Z.; Chou, S. Y. Graphene Transistors Fabricated via Transfer-Printing in Device Active-Areas on Large Wafer. *Nano Lett.* **2007**, *7*, 3840−3844.
(37) Zheng, G.; Chen, Y.; Huang, H.; Zhao, C.; Lu, S.; Chen, S.; Zhang, H.; Wen, S. Improved Transfer Quality of CVD-Grown Graphene by Ultrasonic Processing of Target Substrates: Applications for Ultra-Fast Laser Photonics. *ACS Appl. Mater. Interfaces* **2013**, *5*, 10288−10293.
(38) Sojoudi, H.; Baltazar, J.; Tolbert, L. M.; Henderson, C. L.; Graham, S. Creating Graphene P-n Junctions Using Self-Assembled Monolayers. *ACS Appl. Mater. Interfaces* **2012**, *4*, 4781−4786.
(39) Gorantla, S.; Bachmatiuk, A.; Hwang, J.; Alsalman, H. A.; Kwak, J. Y.; Seyller, T.; Eckert, J.; Spencer, M. G.; Rümmeli, M. H. A Universal Transfer Route for Graphene. *Nanoscale* **2014**, *6*, 889−896.
(40) Martins, L. G. P.; Song, Y.; Zeng, T.; Dresselhaus, M. S.; Kong, J.; Araujo, P. T. Direct Transfer of Graphene onto Flexible Substrates. *Proc. Natl. Acad. Sci. U.S.A.* **2013**, *110*, 17762−17767.
(41) Lee, S.; Lee, S. K.; Kang, C. G.; Cho, C.; Lee, Y. G.; Jung, U.; Lee, B. H. Graphene Transfer in Vacuum Yielding a High Quality Graphene. *Carbon* **2015**, *93*, 286−294.
(42) Feng, X.; Zhang, L.; Ye, Y.; Han, Y.; Xu, Q.; Kim, K.-J.; Ihm, K.; Kim, B.; Bechtel, H.; Martin, M.; Guo, J.; Zhu, J. Engineering the Metal− Organic Interface by Transferring a High-Quality Single Layer Graphene on Top of Organic Materials. *Carbon* **2015**, *87*, 78−86.
(43) Liang, K.; Shu Hui, L.; Turak, A. Probing the Multi-Step Crystallization Dynamics of Micelle Templated Nanoparticles: Structural Evolution of Single Crystalline γ-Fe2O3. *Nanoscale* **2019**, *11*, 9076−9084.
(44) Yu, H.; Turak, A. Nanoreactors or Nanoscale Stablizers: Routes for Solution Processed Indium Tin Oxide Nanoparticles by Reverse Micelle Deposition. *Can. J. Phys.* **2014**, *92*, 797−801.
(45) Hui, L. S.; Munir, M.; Whiteway, E.; Vuong, T. A.; Hilke, M.; Wong, V.; Fanchini, G.; Turak, A. Tunable Etching of CVD Graphene for Transfer Printing of Nanoparticles Driven by Desorption of Contaminants with Low Temperature Annealing. *ECS J. Solid State Sci. Technol.* **2020**, *9*, No. 093006.
(46) Hui, L. S.; Whiteway, E.; Hilke, M.; Turak, A. Synergistic Oxidation of CVD Graphene on Cu by Oxygen Plasma Etching. *Carbon* **2017**, *125*, 500−508.
(47) Hui, L. S.; Whiteway, E.; Hilke, M.; Turak, A. Effect of Post-Annealing on the Plasma Etching of Graphene-Coated-Copper. *Faraday Discuss.* **2014**, *173*, 79−93.
(48) Lin, L.-C.; Grossman, J. C. Atomistic Understandings of Reduced Graphene Oxide as an Ultrathin-Film Nanoporous Membrane for Separations. *Nat. Commun.* **2015**, *6*, No. 8335.
(49) Childres, I.; Jauregui, L. A.; Tian, J.; Chen, Y. P. Effect of Oxygen Plasma Etching on Graphene Studied Using Raman Spectroscopy and Electronic Transport Measurements. *New J. Phys.* **2011**, *13*, No. 025008.
(50) Eckmann, A.; Felten, A.; Mishchenko, A.; Britnell, L.; Krupke, R.; Novoselov, K. S.; Casiraghi, C. Probing the Nature of Defects in Graphene by Raman Spectroscopy. *Nano Lett.* **2012**, *12*, 3925−3930.
(51) Ferrari, A. C.; Meyer, J. C.; Scardaci, V.; Casiraghi, C.; Lazzeri, M.; Mauri, F.; Piscanec, S.; Jiang, D.; Novoselov, K. S.; Roth, S.; Geim, A. K. Raman Spectrum of Graphene and Graphene Layers. *Phys. Rev. Lett.* **2006**, *97*, No. 187401.
(52) Bruna, M.; Ott, A. K.; Ijäs, M.; Yoon, D.; Sassi, U.; Ferrari, A. C. Doping Dependence of the Raman Spectrum of Defected Graphene. *ACS Nano* **2014**, *8*, 7432−7441.
(53) King, A. A. K.; Davies, B. R.; Noorbehesht, N.; Newman, P.; Church, T. L.; Harris, A. T.; Razal, J. M.; Minett, A. I. A New Raman Metric for the Characterisation of Graphene Oxide and Its Derivatives. *Sci. Rep.* **2016**, *6*, No. 19491.
(54) Jung, I.; Vaupel, M.; Pelton, M.; Pinery, R.; Dikin, D. A.; Stankovich, S.; An, J.; Ruoff, R. S. Characterization of Thermally Reduced Graphene Oxide by Imaging Ellipsometry. *J. Phys. Chem. C* **2008**, *112*, 8499−8506.
(55) Beadie, G.; Brindza, M.; Flynn, R. A.; Rosenberg, A.; Shirk, J. S. Refractive Index Measurements of Poly (Methyl Methacrylate) (PMMA) from 0.4 − 1.6μm. *Appl. Opt.* **2015**, *54*, F139−F143.
(56) Bazylewski, P.; Ezugwu, S.; Fanchini, G. A Review of Three-Dimensional Scanning Near-Field Optical Microscopy (3D-SNOM) and Its Applications in Nanoscale Light Management. *Appl. Sci.* **2017**, *7*, No. 973.
(57) Hui, L. S. Comprehensive Characterization of Nanotransfer Printing System for Organic Electronic Devices. Doctoral Thesis, McMaster University: Hamilton, Ontario, 2018.
(58) Willis, H. A.; Zichy, V. J. I.; Hendra, P. J. The Laser-Raman and Infra-Red Spectra of Poly(Methyl Methacrylate). *Polymer* **1969**, *10*, 737−746.
(59) Xingsheng, X.; Hai, M.; Qijing, Z.; Yunsheng, Z. Properties of Raman Spectra and Laser-Induced Birefringence in Polymethyl Methacrylate Optical Fibres. *J. Opt. A: Pure Appl. Opt.* **2002**, *4*, 237−242.
(60) Thomas, K. J.; Sheeba, M.; Nampoori, V. P. N.; Vallabhan, C. P. G.; Radhakrishnan, P. Raman Spectra of Polymethyl Methacrylate Optical Fibres Excited by a 532 Nm Diode Pumped Solid State Laser. *J. Opt. A: Pure Appl. Opt.* **2008**, *10*, No. 055303.
(61) Raja, S. N.; Bekenstein, Y.; Koc, M. A.; Fischer, S.; Zhang, D.; Lin, L.; Ritchie, R. O.; Yang, P.; Alivisatos, A. P. Encapsulation of Perovskite Nanocrystals into Macroscale Polymer Matrices: Enhanced Stability and Polarization. *ACS Appl. Mater. Interfaces* **2016**, *8*, 35523−35533.
(62) Leyden, M. R.; Meng, L.; Jiang, Y.; Ono, L. K.; Qiu, L.; Juarez-Perez, E. J.; Qin, C.; Adachi, C.; Qi, Y. Methylammonium Lead Bromide Perovskite Light-Emitting Diodes by Chemical Vapor Deposition. *J. Phys. Chem. Lett.* **2017**, *8*, 3193−3198.
(63) Kollek, T.; Polarz, S. Facet-Controlled Preparation of Hybrid Perovskite Microcrystals in the Gas Phase and the Remarkable Effect on Optoelectronic Properties. *CrystEngComm* **2017**, *19*, 4615−4621.
(64) Liu, K.-K.; Liu, Q.; Yang, D.-W.; Liang, Y.-C.; Sui, L.-Z.; Wei, J.-Y.; Xue, G.-W.; Zhao, W.-B.; Wu, X.-Y.; Dong, L.; Shan, C.-X. Water-Induced MAPbBr 3@PbBr(OH) with Enhanced Luminescence and Stability. *Light: Sci. Appl.* **2020**, *9*, No. 44.


https://dx.doi.org/10.1021/acsami.0c12178
ACS Appl. Mater. Interfaces 2020, 12, 46530−46538

(65) Turak, A. In *Handbook of Organic Materials for Electronic and Photonic Devices*, 2nd ed.; Ostroverkhova, O., Ed.; Woodhead Publishing Series in Electronic and Optical Materials; Woodhead Publishing, 2019; pp 599−662.
(66) Reese, M. O.; Morfa, A. J.; White, M. S.; Kopidakis, N.; Shaheen, S. E.; Rumbles, G.; Ginley, D. S. Pathways for the Degradation of Organic Photovoltaic P3HT:PCBM Based Devices. *Sol. Energy Mater. Sol. Cells* **2008**, *92*, 746−752.
(67) Arbi, R.; Ibrahim, A.; Liang, K.; Hanta, G.; Shu Hui, L.; Turak, A. Multi-Phase Crystallization from Manipulation of Reverse Micelle Deposition: Tunable Crystal Structure from $\alpha$-Fe2O3 to $\gamma$-Fe2O3 for Single Crystalline Nanoparticles. *Nanoscale* **2020**, No. 003676. NR−ART−05−2020


https://dx.doi.org/10.1021/acsami.0c12178
*ACS Appl. Mater. Interfaces* 2020, 12, 46530−46538